Title: Inferring Synaptic Excitation/Inhibition Balance from Field Potentials

Authors: Richard Gao[1,*], Erik J. Peterson[1], Bradley Voytek[1,2,3,4]

Affiliations:

[1]Department of Cognitive Science, [2]Neurosciences Graduate Program, [3]Institute for Neural Computation, and [4]Kavli Institute for Brain and Mind, University of California, San Diego, La Jolla, CA, USA.

Author Contributions:

R.G., E.J.P., and B.V. initiated and designed the study. R.G., E.J.P., and B.V. developed the computational model. R.G. analyzed the data. All authors discussed the results and wrote the manuscript.

Corresponding Author:

Richard Gao

Department of Cognitive Science, MC 0515

9500 Gilman Drive, La Jolla, CA, 92093-0515

Office: 858-246-2508

rigao@ucsd.edu

Abstract:

Neural circuits sit in a dynamic balance between excitation (E) and inhibition (I). Fluctuations in E:I balance have been shown to influence neural computation, working memory, and information flow, while more drastic shifts and aberrant E:I patterns are implicated in numerous neurological and psychiatric disorders. Current methods for measuring E:I dynamics require invasive procedures that are difficult to perform in behaving animals, and nearly impossible in humans. This has limited the ability to examine the full impact that E:I shifts have in cognition and disease. In this study, we develop a computational model to show that E:I changes can be estimated from the power law exponent (slope) of the electrophysiological power spectrum. Predictions from the model are validated in published data from two species (rats and macaques). We find that reducing E:I ratio via the administration of general anesthetic in macaques results in steeper power spectra, tracking conscious state over time. This causal result is supported by inference from known anatomical E:I changes across the depth of rat hippocampus, as well as oscillatory theta-modulated dynamic shifts in E:I. Our results provide strong evidence that E:I ratio can be readily inferred from electrophysiological recordings at many spatial scales, ranging from the local field potential to surface electrocorticography. This simple method for estimating E:I ratio—one that can be applied retrospectively to existing data—removes a major hurdle in understanding a currently difficult to measure, yet fundamental, aspect of neural computation.

Key Words: excitation-inhibition balance, local field potential, electrocorticography, power spectral density, power law

Introduction

Neurons are constantly bombarded with spontaneous synaptic inputs. This state of fluctuating activity is referred to as the high-conductance state (Destexhe et al., 2003), and gives rise to the asynchronous, irregular (Poisson-like) firing observed *in vivo* (Destexhe et al., 2001). In this state, neural circuits sit in a balance between synaptic excitation (E) and inhibition (I), typically consisting of fast glutamate and slower GABA inputs, respectively, where inhibition is two to six times the strength of excitation (Alvarez and Destexhe, 2004; Xue et al., 2014). Physiologically, the balance of E:I interaction is essential for neuronal homeostasis (Turrigiano and Nelson, 2004) and the formation of neural oscillations (Atallah and Scanziani, 2009). Computationally, E:I balance allows for efficient information transmission and gating (Salinas and Sejnowski, 2001; Vogels and Abbott, 2009), network computation (Mariño et al., 2005), and working memory maintenance (Lim and Goldman, 2013). Conversely, an imbalance between excitation and inhibition, during key developmental periods or tonically thereafter, is implicated in neurological and psychiatric disorders such as epilepsy (González-Ramírez et al., 2015; Symonds, 1959), schizophrenia (Uhlhaas and Singer, 2010), and autism (Dani et al., 2005; Mariani et al., 2015; Rubenstein and Merzenich, 2003), as well as impairments in information processing and social exploration (Yizhar et al., 2011).

Given such a state of intricate balance and its profound consequences when disturbed, quantifying the E:I ratio could aid in better characterizing the functional state of the brain. Existing methods for estimating E:I ratio focus predominantly on interrogation of precisely selected cells, either through identification of excitatory and inhibitory neurons based on extracellular action potential waveforms (Peyrache et al., 2012), or by intracellular voltage-clamp recordings to measure synaptic currents (Monier et al., 2008), often combined with pharmacological or optogenetic manipulations (Reinhold et al., 2015; Xue et al., 2014). These methods are invasive and are restricted

to small populations of cells, making them difficult to apply clinically and to *in vivo* population-level analyses critical for understanding neural network functioning. Other methods, such as magnetic resonance spectroscopy (Henry et al., 2011) and dynamic causal modeling (Legon et al., 2015), are able to provide greater spatial coverage, enabling the sampling of E:I ratio across the brain. However, this gain comes at a cost of temporal resolution – requiring several minutes of data for a single snapshot – and are based on restrictive connectivity assumptions.

Here, we aim to address this important gap in methodology to measure E:I ratio with broad population coverage and fine temporal resolution. Two recent lines of modeling work motivate our starting hypothesis. First, it has been shown that synaptic input fluctuations during the high conductance state can be accurately modeled by a summation of two stationary stochastic processes representing excitatory and inhibitory inputs (Alvarez and Destexhe, 2004). These inputs have different rates of decay, corresponding to a faster AMPA current and a slower $GABA_A$ current, which can be readily differentiated in the frequency domain and computationally inferred from single membrane voltage traces (Pospischil et al., 2009; Fig. 1B). Second, population-level neural field recordings, such as the local field potential (LFP) and electrocorticography (ECoG), have been shown to be primarily dominated by postsynaptic currents (PSC) across large populations (Buzsáki et al., 2012; Mazzoni et al., 2015; Miller et al., 2009). Additionally, recent work by (Haider et al., 2016) observed tight coupling between the LFP and synaptic inputs in the time domain. Thus, we combine these two findings and reason that changes in the relative contribution between excitatory and inhibitory synaptic currents must also be reflected in the field potential, and in particular, in the frequency domain representation (power spectral density, or PSD) of LFP and ECoG recordings. In this work, we derive a straightforward metric that closely tracks E:I ratio via computational modeling, and demonstrate its empirical validity by reanalyzing

publically available databases from two different mammalian species. Specifically, we test the hypotheses that anatomical and theta oscillation-modulated changes in excitation and inhibition in the rat hippocampus can be inferred from CA1 local field potentials, and that anesthesia-induced global inhibition is reflected in macaque cortical electrocorticography.

Materials & Methods

LFP simulation. We simulate local field potentials under the high conductance state (Alvarez and Destexhe, 2004), with the assumption that the LFP is a linear summation of total excitatory and inhibitory currents (Mazzoni et al., 2015). Poisson spike trains from one excitatory and one inhibitory population are generated by integrating interspike intervals (ISI) drawn from independent exponential distributions, with specified mean rate parameter (Fig. 1A). Each spike train is convolved with their respective conductance profiles, which are modeled as a difference-of-exponentials defined by the rise and decay time constants of AMPA and $GABA_A$ receptors (Eq.1, Fig. 1B). Aggregate values for synaptic constants are taken from CNRGlab @ UWaterloo (see *Neurotransmitter Time Constants* in Ref; Table 1). The two resulting time series represent total excitatory (g_E) and inhibitory (g_I) conductances, respectively (Fig. 1C). E:I ratio is defined as the ratio of mean excitatory conductance to mean inhibitory conductance over the simulation time, and specific E:I ratios are achieved by multiplying the inhibitory conductance by a constant, such that mean g_I is 2-6 times mean g_E. To calculate current, conductances are multiplied by the difference between resting potential (-65 mV) and AMPA and $GABA_A$ reversal potential, respectively. Local field potential (LFP), finally, is computed as the summation of the total excitatory and inhibitory current. All simulation parameters are specified in Table 1. Total LFP power is normalized to unity for each E:I ratio.

Equation 1. Difference-of-exponential PSC in time domain

$$\mathrm{PSC(t)} = \mathrm{C}\left(-\mathrm{e}^{\frac{-\mathrm{t}}{\tau_{\mathrm{rise}}}} + \mathrm{e}^{\frac{-\mathrm{t}}{\tau_{\mathrm{decay}}}}\right), \mathrm{C}: \text{amplitude normalization constant}$$

Table 1. LFP Simulation Parameters

Parameter	Value
Population Firing Rate (**E, I**)	2 Hz, 5 Hz
Population Size (**E, I**)	8000, 2000
Resting Membrane Potential	-65 mV
Reversal Potential (AMPA, $GABA_A$)	0 mV, -80 mV
Conductance Rise Time (AMPA, $GABA_A$)	0.1 ms, 0.5 ms
Conductance Decay Time (AMPA, $GABA_A$)	2 ms, 10 ms
E:I Ratio	1:2 to 1:6

Power spectral density (PSD). For all time series data (simulated and recorded LFP, ECoG), the PSD is estimated by computing the median of the square magnitude of the sliding window (short-time) Fourier transform (STFT). The median was used instead of the mean (Welch's method) to account for the non-Gaussian distribution of spectral data, as well as to eliminate the contributions of extreme outliers. All STFT are computed with a window length of 1 second (2-seconds for CA1 data), and an overlap length of 0.25 seconds. A hamming window of corresponding length is applied prior to taking the FFT.

1/f Slope Fitting. To compute the 1/*f* power law exponent (*log-log* slope), we use robust linear regression (MATLAB *robustfit.m*) to find the slope for the line of best fit over specified frequency ranges of the PSD (30-50 Hz, 40-60 Hz for macaque ECoG) (Eq.2).

Equation 2. Log-Log Linear Fit Parameter over Empirical PSD

$$\underset{\mathrm{b},\chi}{\mathrm{argmin}}[\log_{10}\mathrm{PSD} - (\mathrm{b} + \chi\log_{10}\mathrm{F})], \mathrm{F} \in [30,50]\ or\ [40,60]$$

Hippocampal LFP and CA1 depth analysis. LFP data (1250 Hz sampling rate) is recorded in *stratum pyramidale* of CA1 via 4 to 8 shank electrodes (200 um inter-shank distance), with 8 electrodes (160 um^2 area) along the depth of each shank (20-um spacing), perpendicular to the pyramidal cell body layer (Mizuseki et al., 2009). PSD is computed for each electrode as specified above, and 1/f slope extracted. As in Mizuseki et al., 2011, we align the shanks such that the electrode with the maximal ripple power (150-250 Hz) is set to position 0, the middle of *stratum pyramidale*. Other electrodes are vertically translated accordingly. This procedure is repeated for all shanks in every recording (4 rats, 20 sessions total), resulting in slope estimates spanning a depth of 280 um, centered on the pyramidal layer. AMPA and $GABA_A$ synapse densities are adapted from (Megías et al., 2001), for proximal *stratum oriens* and *stratum radiatum* dendrites, and smoothed with a 5-point Gaussian window to produce 15 data points at positions equivalent to LFP electrodes. Spearman correlation is computed by combining slope values at the same depth across all sessions and all rats.

Multivariate Regression Model. Since the synaptic density estimates for E and I are independent but correlated measurements, and E:I ratio is dependent on both previous measures, we built a multivariate regression model to better delineate contributions from the synaptic variables. Combinations of E, I, and E:I ratio were used as predictors, and slope as the predicted variable, and we compute model coefficient, significance, and ordinary and adjusted R^2 values (MATLAB, *LinearModel.fit*).

Theta phase-modulated slope. Theta oscillation is first isolated with a FIR bandpass filter 5-12 Hz, (EEGLAB, *eegfilt.m*). Theta phase is computed as the complex phase angle of the Hilbert transform of the theta oscillation. Segments of theta phase are categorized as peak [-π/2 to π/2, through 0] or trough [π/2 to 3π/2, through π]. Each

corresponding segment in the raw data (~75 samples) is then labeled as peak or trough, Hamming-windowed, and padded to 1250 samples. Average PSD for each phase category is computed as the median of all windowed FFT of the data segments of that category. 1/f slope is then fit to the average PSDs. Per-channel significance statistics are calculated by fitting 1/f slope to each individual cycle STFT for each channel and compared using two-sample *t*-test. To avoid power contamination in the short-time window estimates from observed beta oscillation, LFP data is notch filtered between 15-25 Hz. All results do not change when not filtered for beta, hence are not presented below.

Macaque ECoG During Anesthesia. ECoG data was collected from 2 macaque monkeys during rest, delivery of anesthesia (propofol, 5 & 5.2 mg/kg), and recovery (Yanagawa et al., 2013). PSD was computed for all ECoG channels (n = 128) for each experimental condition and fitted for 1/f slope. Due to clear gamma oscillation near 30 Hz biasing slope estimates, we fit over 40-60 Hz to avoid oscillatory contamination. We then compared slope fit differences at each electrode between conditions (paired-samples *t*-test). Time resolved slope fit was achieved by computing sliding window spectra (absolute value squared of FFT) throughout the duration of the recording (1 s window, 0.25 s step), and a slope estimate was computed for each window. A 15-second median filter was applied to smooth the slope time series plot for Fig. 4D.

All simulation and analysis code can be found at https://github.com/voytekresearch/

Results

E:I ratio drives 1/f changes in simulation

To model LFP under the high conductance state, we simulate an efferent "LFP" population receiving independent Poissonic spike trains from an excitatory and an inhibitory population, as detailed in the Methods. In the frequency domain, we observe that the power spectral density of the LFP (LFP-PSD) follows a decaying (1/*f*) power law for frequencies past 20 Hz (negatively linear in log-log plot), which directly results from adding the two current components, both following power law decays (Fig. 1D). Note that the current-PSDs begin decaying at different frequencies, due to the different rise and decay time constants of AMPA and $GABA_A$ conductance profiles, which have been previously observed in intracellular models of the balanced, high conductance state (Destexhe and Rudolph, 2004).

By changing the relative contributions of excitation and inhibition (E:I ratio), we shift the frequency at which the current-PSDs cross over, which in turn produces different LFP-PSD slopes (power law exponent) in the intermediate frequency range (Fig. 1E). To quantify this relationship, we vary E:I ratio from 1:2 to 1:6, and observe that LFP-PSD slope between 30 to 50 Hz positively correlates with E:I ratio (r = 0.55, p < 0.01; Fig. 1F). The change in slope is restricted to only the low-to-intermediate frequency ranges (below 100 Hz), as we observe a steady decline in correlation between E:I ratio and PSD slope when slope is fitted across shifting, 20-Hz wide frequency windows (Fig. 1G). For subsequent slope analyses, we use a 20-Hz window of the lowest possible frequencies that are above visible oscillatory peaks in the PSD, as a clear drop in correlation is observed when a narrowband oscillation, such as beta (15-25 Hz), is present. Additionally, we avoid high frequency regions because action potentials and firing rate changes have been shown to alter high gamma power at frequencies as low as 50 Hz (Manning et al., 2009; Miller et al., 2007; Ray and Maunsell, 2011). In

summary, our forward LFP model suggests that E:I ratio is monotonically related to LFP-PSD slope in a range between 30-70 Hz, when uncorrupted by oscillatory peaks, and that increasing E:I ratio increases (flattens) PSD slope.

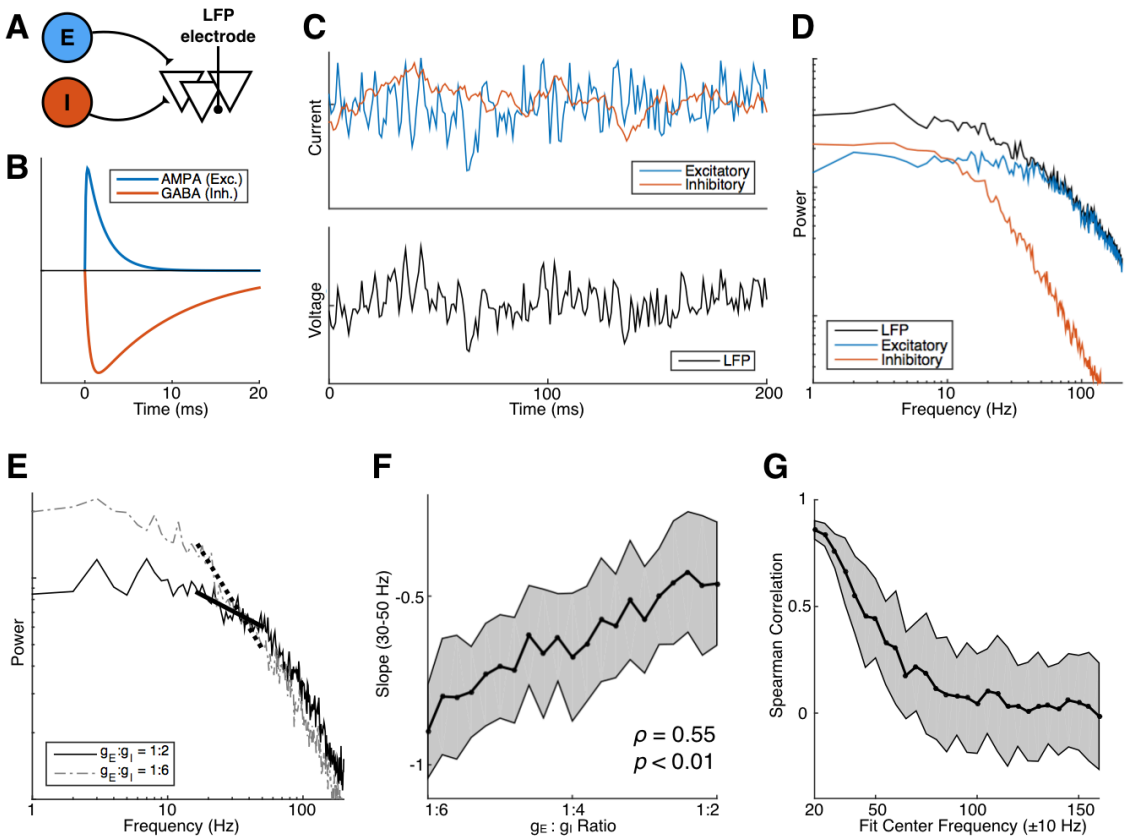

Fig. 1. E:I ratio correlates with PSD slope in simulation.

(A) Model schematic: an "LFP population" receives input from two Poisson populations, one excitatory and one inhibitory. (B) AMPA and $GABA_A$ conductance profiles follow a difference-of-exponentials with different rise and decay time constants. (C) Example time trace of simulated total synaptic currents (top) and LFP (bottom). (D) PSDs of simulated signals in (C). Note power law decays in current-PSDs that begin at different frequencies. (E) Increasing E:I ratio from 1:6 to 1:2 causes a rotation, producing a flatter PSD. (F) E:I ratio is positively correlated with PSD slope between 30-50 Hz. (G) Positive

rank correlations between E:I ratio and PSD slope diminish with increasing frequency of fitting window, up to 100 Hz.

Depth-varying synapse density in rat CA1

To test the relationship between E:I ratio and PSD slope empirically, we first take advantage of the fact that excitatory and inhibitory synapse densities vary along the pyramidal dendrites in the CA1 region of the rat hippocampus (Megías et al., 2001). Given the results of the above modeling experiment, we ask: can changes in the ratio of excitatory to inhibitory synapse density be captured by changes in PSD slope, measured along the depth of CA1? Shank recordings are obtained from CRCNS data portal (Mizuseki et al., 2009), sampling LFP at evenly spaced electrodes across a depth of 280 um centered (*post hoc*, see Methods) on the pyramidal cell layer in CA1 (Fig. 2A). PSDs are computed using data from entire recording sessions of open field foraging (Fig. 2B). PSD slopes are then fitted between 30-50 Hz to arrive at a slope profile that varied across depth (Fig. 2C). To compute E:I ratio, we adapt synapse density values from (Megías et al., 2001) and spatially smooth it to produce data points at equivalent LFP electrode depths (Fig. 2D).

We find that PSD slope across depth is significantly correlated with the AMPA to $GABA_A$ synapse ratio (Spearman's ρ = 0.23, $p < 10^{-5}$), corroborating our *a priori* simulation results (Fig. 2E). Interestingly, inhibitory synapse density alone correlates more strongly with PSD slope (Spearman's ρ = -0.41, $p < 10^{-5}$; Fig. 2F). To further dissect the covariation among the predictor variables, we create multivariate linear models regressing for slope, using every combination of excitatory density, inhibitory density, and E:I density ratio (Table 2). We find that each variable alone produces models that are significantly better than null (constant-only) and with coefficients in the direction expected (positive for E, E:I ratio; negative for I), where the full model with all 3

predictors achieves the highest adjusted R^2. However, inhibitory density in any combination produces the largest increase in adjusted R^2. Thus, we find that PSD slope significantly correlates with E:I ratio in the rat CA1, as measured by synapse density, though the effect is strongly driven by the presence of inhibition.

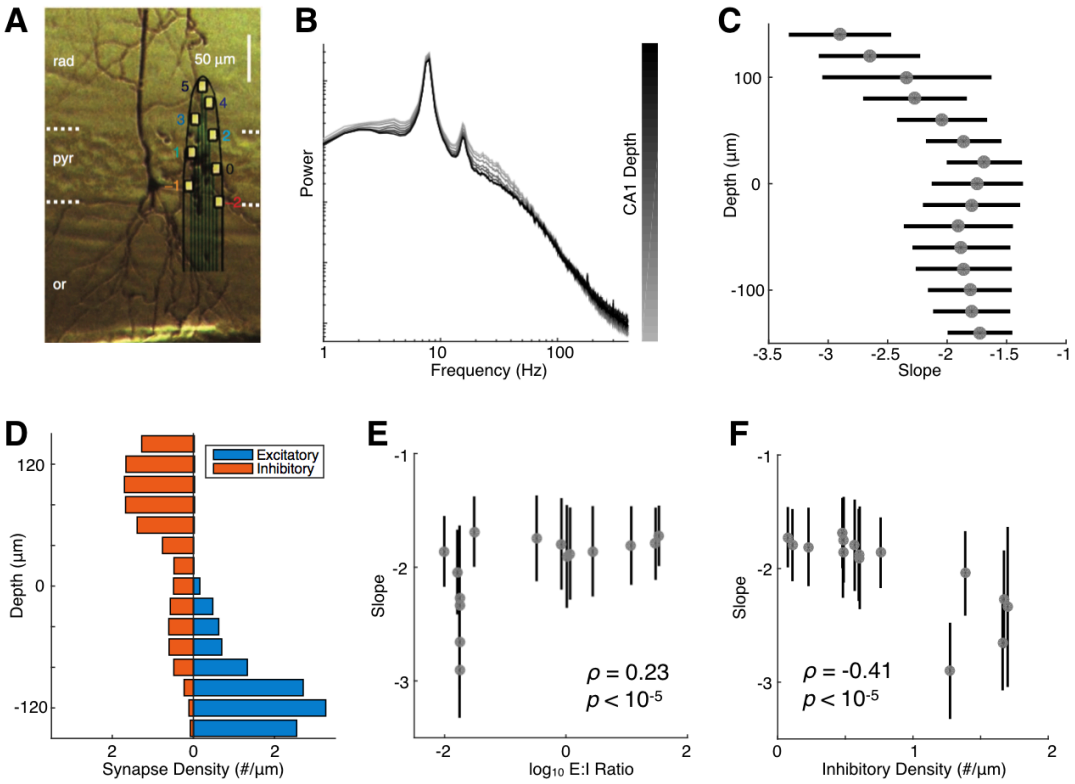

Fig. 2. LFP-PSD slope varies with E:I synapse density ratio in rat CA1.

(A) Example shank spanning across CA1 (*rad*: *stratum radiatum*; *pyr*: *stratum pyramidale*; *or*: *stratum oriens*; adapted from (Mizuseki et al., 2011)). (B) Example PSDs computed from electrodes along one recording shank. (C) Aggregate slope profile across depth, centered to the middle of pyramidal layer (0 µm) (horizontal bars denote standard deviation). (D) Excitatory (AMPA) and inhibitory ($GABA_A$) synapse density varies across CA1 depth. (E and F) LFP-PSD slope correlates positively with E:I

synapse density ratio (E) and negatively with $GABA_A$ density (F) (vertical bars denote standard deviation).

Table 2. Multivariate Linear Model Coefficients and R^2 for Slope vs. E, I, and E:I Ratio. NaNs indicate exclusion of predictor in model.

	Coefficients				R^2	
Model	Constant	E	I	E:I	R-ordinary	R-adjusted
E	-1.9847	0.0848	NaN	NaN	0.0271	0.0261
I	-1.5887	NaN	-0.4509	NaN	0.2231	0.2223
E:I	-1.8612	NaN	NaN	0.1164	0.0730	0.0720
E & I	-1.4601	-0.0890	-0.5478	NaN	0.2426	0.2410
E & E:I	-1.7268	-0.1276	NaN	0.2077	0.0895	0.0875
I & E:I	-1.5339	NaN	-0.5900	-0.0836	0.2395	0.2379
E, I, & E:I	-1.4743	-0.0645	-0.5750	-0.0324	0.2436	0.2412

Theta-modulated cycles of excitation & inhibition

If LFP-PSD slope indeed tracks changes in the balance between excitation and inhibition, it should not only do so statically across space, but dynamically across time as well. Theta oscillation in the rat hippocampus reflects periodic bouts of excitation and inhibition (Buzsáki, 2002). Therefore, we posit that PSD slope would be steeper during the inhibitory phase of theta, and flatter during the excitatory phase. To test this, we use the same CA1 dataset as above, and divide each LFP recording into temporal segments of peak and trough based on theta phase (Fig. 3A; see Methods). Fast Fourier Transforms (FFTs) are computed from these short segments and averaged, showing distinctive slope differences (Fig. 3B).

We find that, across all channels, PSD slope (30-50 Hz) during theta peaks were significantly more negative (steeper) than during theta troughs (paired *t*-test, $p < 10^{-5}$; Fig. 3C and 3D). On a single channel basis, we fit linear slopes to each short segment FFT, and found 844 out of 946 channels with significantly flatter slopes during troughs

(2-sample *t*-test, $p < 10^{-5}$). From this we infer that theta troughs correspond to periods of excitation, which agrees with the biophysical view that negativity in the hippocampal LFP is due to depolarization of membrane potential (Buzsáki et al., 2012). Additionally, we observe that high-frequency (140-230 Hz) power – a surrogate for spiking activity and ripples in the hippocampus (Schomburg et al., 2012) – is higher during theta troughs than peaks, further indicating the correspondence between LFP troughs and windows of excitation (Fig. 3E). Taken together, we find evidence that PSD slope can dynamically track periods of excitation and inhibition facilitated by theta oscillations in the rat hippocampus.

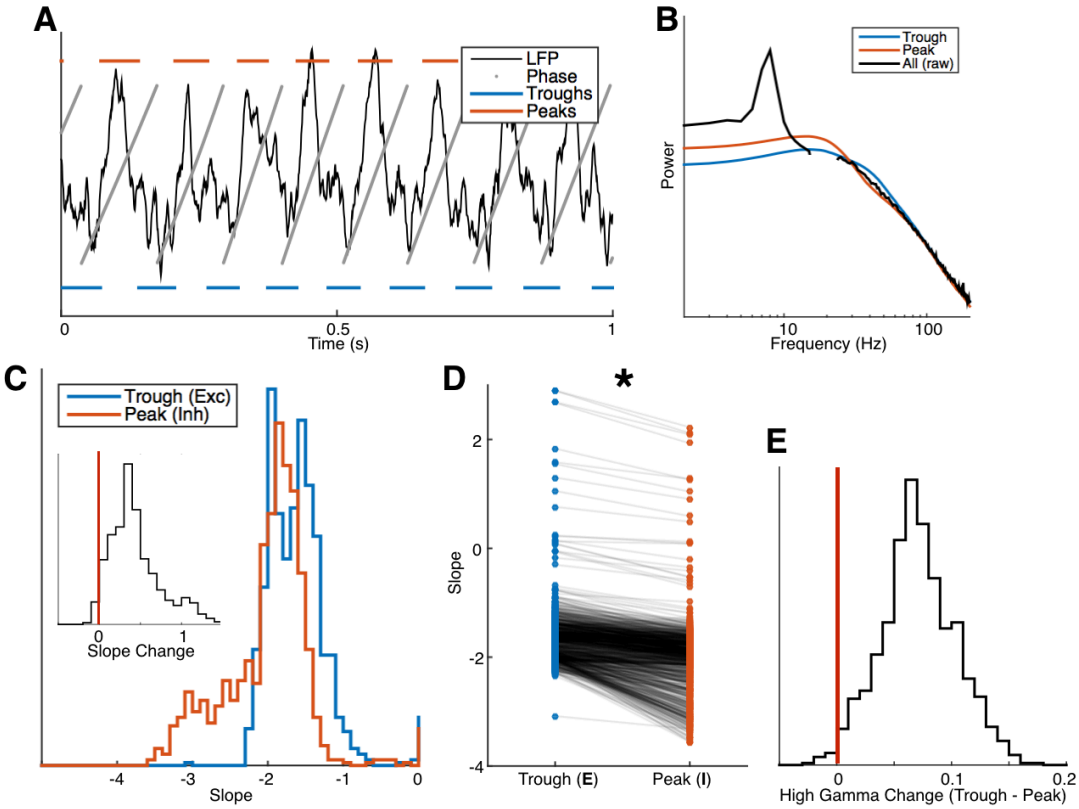

Fig. 3. PSD slope tracks theta-modulated changes in E:I balance.

(A) Schematic of how LFP segments are divided and binned based on theta phase. (B) Example PSD of a single channel over the entire recording (black, notch filter applied in

beta range), and averages across all troughs (blue) and peaks (red) only. (C) Distribution of slope values shifts rightward (more positive) during theta troughs. Inset: distribution of difference in slope (trough minus peak) lies significantly above 0 (vertical red line). (D) Individual-channel comparison of slopes during theta troughs vs. peaks, each channel represented by a pair of connected dots showing nearly universally more negative slope during peaks compared to troughs (* $p < 10^{-5}$). (E) Distribution of difference (trough minus peak) in high frequency activity (HFA, 140-230 Hz) in all channels lies significantly above 0 (vertical red line), indicating an increase in high gamma power from peak to trough.

Propofol-induced increase in $GABA_A$-mediated inhibition

Finally, having shown correlative evidence supporting the hypothesis, we aim to further test the simulation predictions through causal manipulations. Propofol is a general anesthetic that positively modulates the effect of GABA at $GABA_A$ receptors (Concas et al., 1991), effectively decreasing the global E:I ratio. Thus, we query another openly available dataset (http://www.neurotycho.org), in which electrocorticogram (ECoG) from macaques was recorded throughout sedation, to investigate whether ECoG-PSD slope reflects a decrease in E:I ratio induced via pharmacological manipulation (Yanagawa et al., 2013). PSDs are computed for all 128 recording channels per session, for awake resting and anesthetized conditions (Fig. 4A). We observe a significant decrease in PSD slope after onset of anesthesia for all 4 recording sessions (paired *t*-test, all $p < 10^{-5}$, Fig. 4B). The slope decrease is strongest in frontal and temporal electrodes (Fig. 4C), consistent with previous neuroimaging studies spatially locating propofol's region of effect (Zhang et al., 2010). Interestingly, electrodes in the precuneus region show increases in PSD slope during anesthesia instead, suggesting a gain of activity, perhaps due to its situation as a critical, core node within

the default mode network (Utevsky et al., 2014). Finally, to calculate temporally precise demarcations of consciousness state changes, we estimate PSD slope in a time-resolved fashion by fitting over 1-second long sliding FFTs across the entire recording session. We find that PSD slope dynamically tracks the stability of brain state during awake resting, followed by a rapid push towards inhibition after injection that is consistent with propofol's time of onset (15-30 seconds), as well as the slow rebalancing during recovery from anesthesia (Fig. 4D). Unexpectedly, we also observe a rapid increase in slope, back to resting-state values, following the initial gain in inhibition, suggesting a global re-normalization process. Overall, we demonstrate that ECoG-PSD slope dynamically tracks propofol-induced gain in inhibition consistently across brain regions and time.

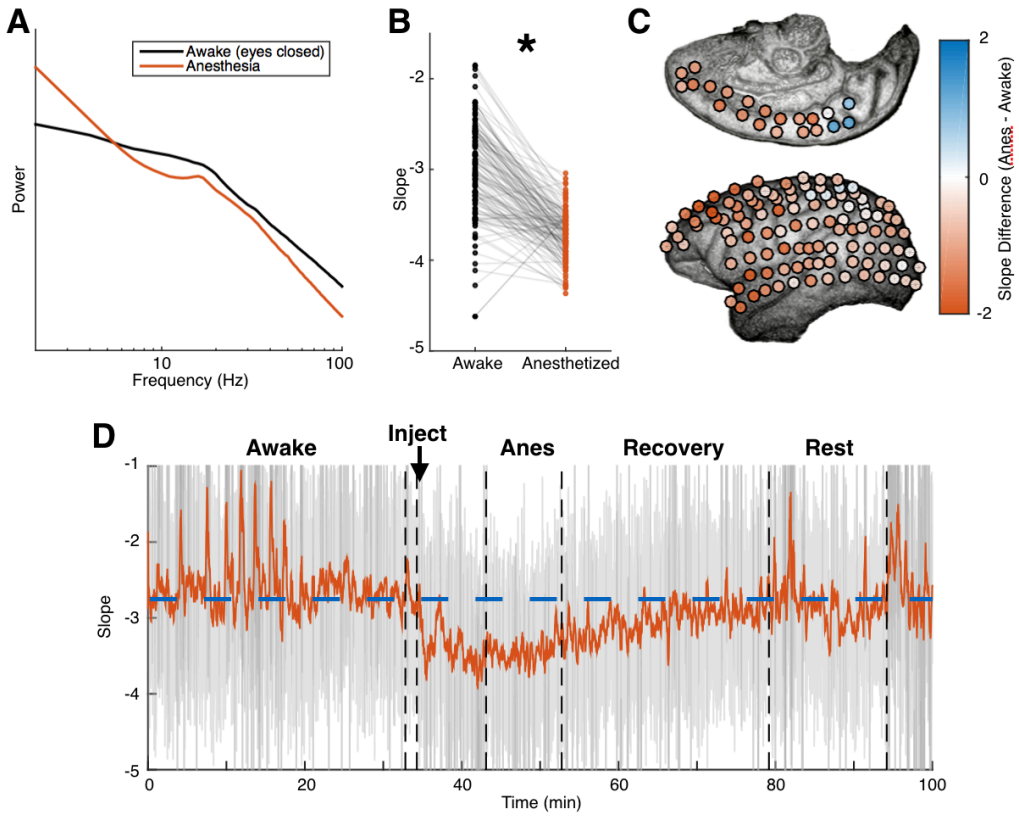

Fig. 4. ECoG-PSD slope tracks propofol-induced global inhibition.

(A) Average PSD across all channels during resting (black) and anesthetized (red) show distinct slope differences beyond 30 Hz. (B) Significant slope decrease is observed during anesthesia (pair *t*-test, * $p < 10^{-5}$). (C) Slope decrease is observed across most of cortex, most prominently in the frontal and temporal areas. Slope increase is observed exclusively in the precuneus. (D) Time-resolved estimate of PSD slope tracks, with fine temporal resolution, changes in brain state from awake to anesthetized (Anes), and as well as a slow recovery to baseline rest levels (marked by dashed blue line). Grey, unsmoothed; red, 15s smoothing window applied.

DISCUSSION

Guided by predictions from our computational modeling results, our analyses of existing datasets from two mammalian species with different experimental manipulations and recording equipment demonstrate that information about local E:I ratio can be robustly captured from the spectral representation of electrophysiological signals. Specifically, we show that LFP-PSD slope correlates with both anatomical E:I ratio—represented by changes in synaptic density ratio across CA1 layers—and dynamic E:I ratio as modulated by theta oscillation in the rat hippocampus. In addition, ECoG-PSD slope tracks the increase of inhibition in non-human primate brains induced by propofol, across brain regions and time.

Evidence that spiking can be partially extracted from the broadband (2-250 Hz) or high gamma (>80 Hz) spectral power of meso-/macro-scale neural recordings (LFP, ECoG) provided an important link between local neuronal activity and the LFP, opening numerous avenues of research (Manning et al., 2009; Miller et al., 2009; Mukamel et al., 2005). In contrast to the copious literature regarding broadband/high gamma, much of the work on E:I balance has been limited to intracellular recordings, methods with limited temporal resolution, multiple single-unit recordings, or optogenetic manipulations. Given the broad and important role that E:I balance plays in neural computation, information transfer, and oscillatory and homeostatic mechanisms, the inability to easily measure E:I parameters at a large scale has hindered basic and clinical research. To this end, we develop a simple metric that can be applied at different intracranial recording scales, which can potentially be extended to extracranial EEG recordings, with profound implications for clinical and basic science research.

Limitations

There are several caveats in this study worth noting. Most notably is the underlying assumption that LFP and ECoG are solely composed of AMPA and $GABA_A$ synaptic currents. In reality, LFP reflects the integration of all ionic currents, including action potentials (Schomburg et al., 2012) – which shift the broadband/high gamma frequencies (Manning et al., 2009; Miller et al., 2009; Mukamel et al., 2005) – and slow glial currents (Buzsáki et al., 2012). The computational model also makes several assumptions, such as homogeneous-rate spiking and constant PSC waveforms, as well as excluding biophysical details like 3D arrangement of the spiking population. These factors will certainly influence the overall shape of the PSD, although this class of LFP model we employ was shown to best approximate neuronal networks with 3D cellular morphology (Mazzoni et al., 2015). Additionally, such models have been used to capture the aforementioned broadband/high gamma relationship to spiking activity (Miller et al., 2009), a phenomenon that is also reproduced in our model through an overall (and equivalent) increase in firing rate from both excitatory and inhibitory populations.

Furthermore, although our computational model makes predictions that EI balance can be captured from the 1/f slope, we emphasize that our model assumes a linear independent summation of E and I currents that do not account for the fast-coupling or recurrent nature of cortical circuits. This assumption rests on the high-conductance state of cortical circuits over long recording lengths, effectively washing out stimulus-specific frequency response. So while our simple slope-fitting model captures significant variance in E:I ratio, the fact that the feedback engagement of E and I makes these two contributions inextricably linked suggests that more sophisticated models would perform better when the superposition assumption does not satisfy. In particular, previous works have shown that the amplitude of the power spectrum depends critically on this interaction in similar frequency ranges used in our analyses to infer E:I from the

spectral slope, when considering time-inhomogeneous stimuli (Brunel and Wang, 2003; Mazzoni et al., 2008). Some methods have been proposed to estimate network parameters (including E:I ratio) when recurrent E:I interactions are taken into account (Barbieri et al., 2014). These methods are more complicated than, but complementary to, the model we propose, and they may be preferable when considering non-stationary, stimulus-evoked responses.

Finally, because non-neural sources such as the amplifier, reference scheme, and ambient noise can affect spectral slope, slope-inferred E:I ratio should only be interpreted in the context of a comparative experimental design in which the relative E:I ratio can be interrogated in response to experimental manipulations or population differences, rather than ascribing meaning to the exact value of the slope itself. In particular, it has been shown that different referencing schemes, such as bipolar vs. common-average, have profound effects on the measured PSD slope (Shirhatti et al., 2016). In addition, we observe that PSD slope of cortical ECoG is much more negative than that of CA1 LFP recordings, which, in turn, is lower than slopes produced by our LFP model, suggesting that anatomical differences and dendritic integration process all contribute to the measured slope (Lindén et al., 2010; Pettersen et al., 2014).

Power Law (1/f) Decay in Neural Recordings

Power law exponent (slope) changes of the PSD ("rotation") have recently been observed in several empirical studies, linking it to changes in global awake and sleep states (He et al., 2010), age-related cognitive decline (Voytek and Knight, 2015; Voytek et al., 2015; Waschke et al., 2017.) and visuomotor task-related activation (Podvalny et al., 2015). The *1/f* power law nature of neural recordings has been interpreted within a self-organized criticality framework (Bak et al., 1987; He et al., 2010), with general anesthesia argued to alter the criticality of self-organized brain networks (Alonso et al.,

2014). It has been shown, however, that power law statistics do not imply criticality in neuronal networks (Touboul and Destexhe, 2010), and the finding that neuronal activity exhibit power law statistics at all has been questioned (Bédard et al., 2006). Furthermore, many previous reports ignore or overlook the fact that PSD of neural recordings are not 1/f at all frequencies and do not have a constant power law exponent – both requirements in the self-organized criticality framework. Instead, LFP and ECoG PSDs often have relatively constant spectral power at low frequencies between 1-10 Hz, as well as different power law exponents at different frequencies. For example, ultra-low frequency region (<1 Hz) was posited to exhibit 1/f decay due to recurrent network activity (Chaudhuri et al., 2016), and power law in the very high frequency (>200 Hz) was shown to be a result of stochastic fluctuations in ion channels (Diba et al., 2004).

Our model and results reconcile the 1/*f* and low-frequency plateau observation by the simple fact that the spectral representation of synaptic currents (Lorentzian) takes on that shape (Fig. 1D), as others have noted before (Destexhe and Rudolph, 2004). In fact, previous works have modeled the Lorentzian form as due to the network propagation time constant of a recurrent excitatory population (Freeman and Zhai, 2009) and excitatory synaptic time constants coupled with dendritic filtering (Miller et al., 2009). However, recent evidence suggests that synaptic inhibition also plays a significant role in shaping the LFP time series (Telenczuk et al., 2017). As such, we infer that the balance between excitation and inhibition could be extracted from the extracellular field potential, though not from the polarity of the time series signal itself. Hence, we propose that slope changes in a particular frequency region (30-70 Hz) correspond to changes in E:I balance, while making no claims about other frequency regions, and our multivariate model in the CA1 analysis reveals that both inhibition alone and E:I ratio predict spectral slope better than excitation alone. Altogether, it follows that different processes may give

rise to power law phenomenon at different temporal scales, hence different frequency ranges (Chaudhuri et al., 2016). Our observations here do not negate the criticality perspective, but reframes it in E:I terms, wherein constant E:I balancing is crucial for maintaining neuronal excitability at a critical state (Xue et al., 2014).

In summary, our results overturn a long-standing challenge that the relative contributions of EPSCs and IPSCs to electrophysiological signals cannot be inferred (Yizhar et al., 2011). We show that this limitation can be overcome using relatively simple metrics derived from meso- and macro-scale neural recordings, and that it can be easily applied retrospectively to existing data, opening new domains of inquiry and allowing for reanalyses within an E:I framework. Furthermore, our results provide insights into several ongoing research domains, such as possible contributors to the *1/f* power law phenomenon often observed in field potential power spectra. By providing a new way for decoding the physiological information of the aggregate field potential, we can query brain states in novel ways, helping close the gap between cellular and cognitive neuroscience and increasing our ability to relate fundamental brain processes to behaviour and cognition as a result.

Acknowledgements

We thank S.R. Cole, T. Donoghue, C. Holdgraf, R. van der Meij, E. Mukamel, D. Nitz, T. Noto, J. Olson, B. Postle, and T. Tran for invaluable discussion and comments, the Buzsáki Lab and CRCNS for their public repository of rat LFP data, and the Fujii Lab and NeuroTycho for their public repository of monkey ECoG data. B.V. is supported by the University of California, San Diego, Qualcomm Institute, California Institute for Telecommunications and Information Technology, Strategic Research Opportunities Program, and a Sloan Research Fellowship. R.G is supported by NSERC PGS-D, the

Katzin Prize, and Frontiers of Innovation Scholars Program at the University of California, San Diego. The authors declare no conflicts of interest.

REFERENCES

Alonso, L.M., Proekt, A., Schwartz, T.H., Pryor, K.O., Cecchi, G.A., Magnasco, M.O., 2014. Dynamical criticality during induction of anesthesia in human ECoG recordings. Front Neural Circuits 8, 20. doi:10.3389/fncir.2014.00020

Alvarez, F.P., Destexhe, A., 2004. Simulating cortical network activity states constrained by intracellular recordings. Neurocomputing 285–290. doi:10.1016/j.neucom.2004.01.057

Atallah, B.V., Scanziani, M., 2009. Instantaneous modulation of gamma oscillation frequency by balancing excitation with inhibition. Neuron 62, 566–577. doi:10.1016/j.neuron.2009.04.027

Bak, P., Tang, C., Wiesenfeld, K., 1987. Self-organized criticality: An explanation of the 1/*f* noise. Physical Review Letters 59, 381–384. doi:10.1103/PhysRevLett.59.381

Barbieri, F., Mazzoni, A., Logothetis, N.K., Panzeri, S., Brunel, N., 2014. Stimulus dependence of local field potential spectra: experiment versus theory. J. Neurosci. 34, 14589–14605. doi:10.1523/JNEUROSCI.5365-13.2014

Bédard, C., Kröger, H., Destexhe, A., 2006. Does the 1/f frequency scaling of brain signals reflect self-organized critical states? Physical Review Letters 97. doi:10.1103/PhysRevLett.97.118102

Brunel, N., Wang, X.-J., 2003. What determines the frequency of fast network oscillations with irregular neural discharges? I. Synaptic dynamics and excitation-inhibition balance. J. Neurophysiol. 90, 415–430. doi:10.1152/jn.01095.2002

Buzsáki, G., 2002. Theta Oscillations in the Hippocampus. Neuron 33, 325–340. doi:10.1016/S0896-6273(02)00586-X

Buzsáki, G., Anastassiou, C.A., Koch, C., 2012. The origin of extracellular fields and currents--EEG, ECoG, LFP and spikes. Nat Rev Neurosci 13, 407–420. doi:10.1038/nrn3241

Chaudhuri, R., He, B., Wang, X.-J., 2016. Random recurrent networks near criticality capture the broadband power distribution of human ECoG dynamics, bioRxiv. doi:10.1101/036228

Concas, A., Santoro, G., Serra, M., Sanna, E., Biggio, G., 1991. Neurochemical action of

the general anaesthetic propofol on the chloride ion channel coupled with GABAA receptors. Brain Res. 542, 225–232.

Dani, V.S., Chang, Q., Maffei, A., Turrigiano, G.G., Jaenisch, R., Nelson, S.B., 2005. Reduced cortical activity due to a shift in the balance between excitation and inhibition in a mouse model of Rett Syndrome. Proc Natl Acad Sci USA 102, 12560–12565. doi:10.1073/pnas.0506071102

Destexhe, A., Rudolph, M., 2004. Extracting information from the power spectrum of synaptic noise. J Comput Neurosci 17, 327–345. doi:10.1023/B:JCNS.0000044875.90630.88

Destexhe, A., Rudolph, M., Fellous, J.M., Sejnowski, T.J., 2001. Fluctuating synaptic conductances recreate in vivo-like activity in neocortical neurons. Neuroscience 107, 13–24.

Destexhe, A., Rudolph, M., Paré, D., 2003. The high-conductance state of neocortical neurons in vivo. Nat Rev Neurosci 4, 739–751. doi:10.1038/nrn1198

Diba, K., Lester, H.A., Koch, C., 2004. Intrinsic noise in cultured hippocampal neurons: experiment and modeling. J. Neurosci. 24, 9723–9733. doi:10.1523/JNEUROSCI.1721-04.2004

Freeman, W.J., Zhai, J., 2009. Simulated power spectral density (PSD) of background electrocorticogram (ECoG). Cogn Neurodyn 3, 97–103. doi:10.1007/s11571-008-9064-y

González-Ramírez, L.R., Ahmed, O.J., Cash, S.S., Wayne, C.E., Kramer, M.A., 2015. A biologically constrained, mathematical model of cortical wave propagation preceding seizure termination. PLoS Comput Biol 11, e1004065. doi:10.1371/journal.pcbi.1004065

Haider, B., Schulz, D.P.A., Häusser, M., Carandini, M., 2016. Millisecond Coupling of Local Field Potentials to Synaptic Currents in the Awake Visual Cortex. Neuron 90, 35–42. doi:10.1016/j.neuron.2016.02.034

He, B.J., Zempel, J.M., Snyder, A.Z., Raichle, M.E., 2010. The temporal structures and functional significance of scale-free brain activity. Neuron 66, 353–369. doi:10.1016/j.neuron.2010.04.020

Henry, M.E., Lauriat, T.L., Shanahan, M., Renshaw, P.F., Jensen, J.E., 2011. Accuracy and stability of measuring GABA, glutamate, and glutamine by proton magnetic resonance spectroscopy: a phantom study at 4 Tesla. J. Magn. Reson. 208, 210–218. doi:10.1016/j.jmr.2010.11.003

Legon, W., Punzell, S., Dowlati, E., Adams, S.E., Stiles, A.B., Moran, R.J., 2015. Altered Prefrontal Excitation/Inhibition Balance and Prefrontal Output: Markers of Aging in Human Memory Networks. Cereb. Cortex. doi:10.1093/cercor/bhv200

Lim, S., Goldman, M.S., 2013. Balanced cortical microcircuitry for maintaining information in working memory. Nat Neurosci 16, 1306–1314. doi:10.1038/nn.3492

Lindén, H., Pettersen, K.H., Einevoll, G.T., 2010. Intrinsic dendritic filtering gives low-pass power spectra of local field potentials. J Comput Neurosci 29, 423–444. doi:10.1007/s10827-010-0245-4

Manning, J.R., Jacobs, J., Fried, I., Kahana, M.J., 2009. Broadband shifts in local field potential power spectra are correlated with single-neuron spiking in humans. J. Neurosci. 29, 13613–13620. doi:10.1523/JNEUROSCI.2041-09.2009

Mariani, J., Coppola, G., Zhang, P., Abyzov, A., Provini, L., Tomasini, L., Amenduni, M., Szekely, A., Palejev, D., Wilson, M., Gerstein, M., Grigorenko, E.L., Chawarska, K., Pelphrey, K.A., Howe, J.R., Vaccarino, F.M., 2015. FOXG1-Dependent Dysregulation of GABA/Glutamate Neuron Differentiation in Autism Spectrum Disorders. Cell 162, 375–390. doi:10.1016/j.cell.2015.06.034

Mariño, J., Schummers, J., Lyon, D.C., Schwabe, L., Beck, O., Wiesing, P., Obermayer, K., Sur, M., 2005. Invariant computations in local cortical networks with balanced excitation and inhibition. Nat Neurosci 8, 194–201. doi:10.1038/nn1391

Mazzoni, A., Lindén, H., Cuntz, H., Lansner, A., Panzeri, S., Einevoll, G.T., 2015. Computing the Local Field Potential (LFP) from Integrate-and-Fire Network Models. PLoS Comput Biol 11, e1004584. doi:10.1371/journal.pcbi.1004584

Mazzoni, A., Panzeri, S., Logothetis, N.K., Brunel, N., 2008. Encoding of naturalistic stimuli by local field potential spectra in networks of excitatory and inhibitory neurons. PLoS Comput Biol 4, e1000239. doi:10.1371/journal.pcbi.1000239

Megías, M., Emri, Z., Freund, T.F., Gulyás, A.I., 2001. Total number and distribution of inhibitory and excitatory synapses on hippocampal CA1 pyramidal cells. Neuroscience 102, 527–540.

Miller, K.J., Leuthardt, E.C., Schalk, G., Rao, R.P.N., Anderson, N.R., Moran, D.W., Miller, J.W., Ojemann, J.G., 2007. Spectral changes in cortical surface potentials during motor movement. J. Neurosci. 27, 2424–2432. doi:10.1523/JNEUROSCI.3886-06.2007

Miller, K.J., Sorensen, L.B., Ojemann, J.G., Nijs, den, M., 2009. Power-law scaling in the brain surface electric potential. PLoS Comput Biol 5, e1000609.

doi:10.1371/journal.pcbi.1000609

Mizuseki, K., Diba, K., Pastalkova, E., Buzsáki, G., 2011. Hippocampal CA1 pyramidal cells form functionally distinct sublayers. Nat Neurosci 14, 1174–1181. doi:10.1038/nn.2894

Mizuseki, K., Sirota, A., Pastalkova, E., Buzsaki, G., 2009. Multi-unit recordings from the rat hippocampus made during open field foraging. Available online at: CRCNS. org.

Monier, C., Fournier, J., Frégnac, Y., 2008. In vitro and in vivo measures of evoked excitatory and inhibitory conductance dynamics in sensory cortices. Journal of Neuroscience Methods 169, 323–365. doi:10.1016/j.jneumeth.2007.11.008

Mukamel, R., Gelbard, H., Arieli, A., Hasson, U., Fried, I., Malach, R., 2005. Coupling between neuronal firing, field potentials, and FMRI in human auditory cortex. Science 309, 951–954. doi:10.1126/science.1110913

Pettersen, K.H., Lindén, H., Tetzlaff, T., Einevoll, G.T., 2014. Power laws from linear neuronal cable theory: power spectral densities of the soma potential, soma membrane current and single-neuron contribution to the EEG. PLoS Comput Biol 10, e1003928. doi:10.1371/journal.pcbi.1003928

Peyrache, A., Dehghani, N., Eskandar, E.N., Madsen, J.R., Anderson, W.S., Donoghue, J.A., Hochberg, L.R., Halgren, E., Cash, S.S., Destexhe, A., 2012. Spatiotemporal dynamics of neocortical excitation and inhibition during human sleep. Proc Natl Acad Sci USA 109, 1731–1736. doi:10.1073/pnas.1109895109

Podvalny, E., Noy, N., Harel, M., Bickel, S., Chechik, G., Schroeder, C.E., Mehta, A.D., Tsodyks, M., Malach, R., 2015. A unifying principle underlying the extracellular field potential spectral responses in the human cortex. J. Neurophysiol. 114, 505–519. doi:10.1152/jn.00943.2014

Pospischil, M., Piwkowska, Z., Bal, T., Destexhe, A., 2009. Extracting synaptic conductances from single membrane potential traces. Neuroscience 158, 545–552. doi:10.1016/j.neuroscience.2008.10.033

Ray, S., Maunsell, J.H.R., 2011. Network rhythms influence the relationship between spike-triggered local field potential and functional connectivity. J. Neurosci. 31, 12674–12682. doi:10.1523/JNEUROSCI.1856-11.2011

Reinhold, K., Lien, A.D., Scanziani, M., 2015. Distinct recurrent versus afferent dynamics in cortical visual processing. Nat Neurosci 18, 1789–1797. doi:10.1038/nn.4153

Rubenstein, J., Merzenich, M.M., 2003. Model of autism: increased ratio of excitation/inhibition in key neural systems. Genes Brain Behav. 2, 255–267.

doi:10.1046/j.1601-183X.2003.00037.x

Salinas, E., Sejnowski, T.J., 2001. Correlated neuronal activity and the flow of neural information. Nat Rev Neurosci 2, 539–550. doi:10.1038/35086012

Schomburg, E.W., Anastassiou, C.A., Buzsáki, G., Koch, C., 2012. The spiking component of oscillatory extracellular potentials in the rat hippocampus. J. Neurosci. 32, 11798–11811. doi:10.1523/JNEUROSCI.0656-12.2012

Shirhatti, V., Borthakur, A., Ray, S., 2016. Effect of Reference Scheme on Power and Phase of the Local Field Potential. Neural Comput 28, 882–913. doi:10.1162/NECO_a_00827

Symonds, C., 1959. Excitation and Inhibition in Epilepsy. Brain 82, 133–146. doi:10.1093/brain/82.2.133

Telenczuk, B., Dehghani, N., Le Van Quyen, M., Cash, S.S., Halgren, E., Hatsopoulos, N.G., Destexhe, A., 2017. Local field potentials primarily reflect inhibitory neuron activity in human and monkey cortex. Sci Rep 7. doi:10.1038/srep40211

Touboul, J., Destexhe, A., 2010. Can power-law scaling and neuronal avalanches arise from stochastic dynamics? PLoS ONE. doi:10.1371/journal.pone.0008982.g001

Turrigiano, G.G., Nelson, S.B., 2004. Homeostatic plasticity in the developing nervous system. Nat Rev Neurosci 5, 97–107. doi:10.1038/nrn1327

Uhlhaas, P.J., Singer, W., 2010. Abnormal neural oscillations and synchrony in schizophrenia. Nat Rev Neurosci 11, 100–113. doi:10.1038/nrn2774

Utevsky, A.V., Smith, D.V., Huettel, S.A., 2014. Precuneus Is a Functional Core of the Default-Mode Network. Journal of Neuroscience 34, 932–940. doi:10.1523/JNEUROSCI.4227-13.2014

Vogels, T.P., Abbott, L.F., 2009. Gating multiple signals through detailed balance of excitation and inhibition in spiking networks. Nat Neurosci 12, 483–491. doi:10.1038/nn.2276

Voytek, B., Knight, R.T., 2015. Dynamic network communication as a unifying neural basis for cognition, development, aging, and disease. Biol. Psychiatry 77, 1089–1097. doi:10.1016/j.biopsych.2015.04.016

Voytek, B., Kramer, M.A., Case, J., Lepage, K.Q., Tempesta, Z.R., Knight, R.T., Gazzaley, A., 2015. Age-Related Changes in 1/f Neural Electrophysiological Noise. J. Neurosci. 35, 13257–13265. doi:10.1523/JNEUROSCI.2332-14.2015

Waschke, L., Woestmann, M., Obleser, J., 2017. Neural noise in the age-varying human brain predicts perceptual decisions. doi:10.1101/103432

Xue, M., Atallah, B.V., Scanziani, M., 2014. Equalizing excitation-inhibition ratios across visual cortical neurons. Nature 511, 596–600. doi:10.1038/nature13321

Yanagawa, T., Chao, Z.C., Hasegawa, N., Fujii, N., 2013. Large-scale information flow in conscious and unconscious states: an ECoG study in monkeys. PLoS ONE 8, e80845. doi:10.1371/journal.pone.0080845

Yizhar, O., Fenno, L.E., Prigge, M., Schneider, F., Davidson, T.J., O'Shea, D.J., Sohal, V.S., Goshen, I., Finkelstein, J., Paz, J.T., Stehfest, K., Fudim, R., Ramakrishnan, C., Huguenard, J.R., Hegemann, P., Deisseroth, K., 2011. Neocortical excitation/inhibition balance in information processing and social dysfunction. Nature 477, 171–178. doi:10.1038/nature10360

Zhang, H., Wang, W., Zhao, Z., Ge, Y., Zhang, J., Yu, D., Chai, W., Wu, S., Xu, L., 2010. The action sites of propofol in the normal human brain revealed by functional magnetic resonance imaging. Anat Rec (Hoboken) 293, 1985–1990. doi:10.1002/ar.21069